

DRAFT

CMS Paper

The content of this note is intended for CMS internal use and distribution only

2011/10/16
Head Id: 79712
Archive Id: 81104:81200M
Archive Date: 2011/09/28
Archive Tag: trunk

Measurement of the Production Cross Section of Pairs of Isolated Photons in pp collisions at $\sqrt{s} = 7$ TeV

The CMS Collaboration

Abstract

The integrated and differential cross sections of the production of pairs of isolated photons have been measured in proton-proton collisions at a centre-of-mass energy of 7 TeV with the CMS detector at the LHC. Data corresponding to an integrated luminosity of 36 pb^{-1} have been analysed. A next-to-leading-order perturbative QCD calculation is compared to the measurements. A discrepancy is observed for regions of the phase space with small angle between the two emitted photons.

This box is only visible in draft mode. Please make sure the values below make sense.

PDFAuthor: S. Ahuja, O. Bondu, H. Brun, N. Chanon, G. Chen, B. Choudary, M. Dejardin, D. D'Enterria, J. Fan, F. Ferri, S. Gascon-Shotkin, P. Gras, M. Lethuillier, J. Malcles, L. Millischer, J. Tao, H. Xiao
PDFTitle: Measurement of the Isolated Diphoton Cross Section in CMS at $\sqrt{s}=7$ TeV
PDFSubject: CMS
PDFKeywords: CMS, physics, software, computing

Please also verify that the abstract does not use any user defined symbols

1 Introduction

The study of the production of energetic photon pairs in hadronic collisions is a valuable testing ground of the perturbative Quantum Chromodynamics (pQCD). The emission from hard parton-parton scattering of a pair of photons constitutes a particularly clean test of perturbation theory in the collinear- [1, 2] and k_T - [3] factorisation approaches, as well as of soft gluon logarithmic resummation techniques [4]. A comprehensive understanding of photon pair production is also important as it represents a major background to certain searches for rare or exotic processes, such as the production of a light Higgs boson, extra-dimension gravitons, and some supersymmetric states.

This paper presents a measurement of the production cross section of isolated photon pairs in proton-proton collisions at a centre-of-mass energy of $\sqrt{s} = 7$ TeV using the Compact Muon Solenoid (CMS) detector at the Large Hadron Collider (LHC). Photons produced in the hard scattering of quarks and gluons, called prompt, and isolated, are henceforth simply referred to as *signal photons* and the rest of the photons as *background photons*. A pair of signal photons will be referred to as a diphoton. The data sample was collected in 2010 and corresponds to an integrated luminosity of 36.0 pb^{-1} . Recent diphoton cross-section measurements have been performed by the D0 [5] and CDF [6, 7] collaborations, at the Tevatron proton-antiproton collider at $\sqrt{s} = 1.96$ TeV, and by the ATLAS collaboration at the LHC [8].

The CMS detector consists of a silicon pixel and strip tracker surrounded by a crystal electromagnetic calorimeter (ECAL) and by a brass-scintillator sampling hadron calorimeter (HCAL), all in an axial 3.8 T magnetic field provided by a superconducting solenoid of 6 m internal diameter. The gas-ionization detectors of the muon system are embedded in the steel return yoke of the magnet, in a field of 1.9 T. In addition to the barrel and endcap detectors, CMS has an extensive forward calorimetry system. A more detailed description of CMS can be found elsewhere [9].

In the CMS coordinate system, θ and φ respectively designate the polar angle with respect to the counterclockwise beam direction and the azimuthal angle, expressed in radians throughout this paper. The pseudorapidity is defined as $\eta = -\ln \tan \frac{\theta}{2}$.

The distance in the (η, φ) plane is defined as $R = \sqrt{(\Delta\eta)^2 + (\Delta\varphi)^2}$. The transverse energy E_T of a particle is defined as $E_T = E \sin \theta$, where E is the energy of the particle. Its rapidity is defined as $y = \frac{1}{2} \ln \frac{E+p_z}{E-p_z}$, with p_z its longitudinal momentum with respect to the beam axis. Its transverse momentum is denoted p_T , $p_T = p \sin \theta$.

The electromagnetic calorimeter, which plays a major role in this measurement, consists of nearly 76 000 lead tungstate crystals. It is divided into a central part (barrel) covering the region $|\eta| < 1.48$ and a forward part (endcaps) extending the coverage up to $|\eta| < 3$ for a particle originating from the nominal interaction point. The crystals are arranged in a projective geometry with a granularity of 0.0174 in both the η and φ directions in the barrel, and increasing with η from 0.021 to 0.050 in the endcaps. A preshower detector consisting of two planes of silicon sensors interleaved, with a total radiation length $3X_0$ of lead, is placed in front of the endcaps to cover the pseudorapidity region $1.65 < |\eta| < 2.6$.

The differential cross section is measured as a function of variables which are particularly relevant in searches for rare processes or to characterise QCD interactions (see e.g. [2]):

- the diphoton invariant mass, $m_{\gamma\gamma}$;
- the azimuthal angle between the two photons, $\Delta\varphi_{\gamma\gamma}$;

- 45 • the transverse momentum of the photon pair, $p_{T,\gamma\gamma} = \sqrt{p_{T,\gamma_1}^2 + p_{T,\gamma_2}^2 + 2 p_{T,\gamma_1} p_{T,\gamma_2} \cos \Delta\phi_{\gamma\gamma}}$,
- 46 where p_{T,γ_1} and p_{T,γ_2} are the magnitudes of the transverse momenta of the two pho-
- 47 tons;
- 48 • and $\cos \theta^* = \tanh \frac{\Delta y_{\gamma\gamma}}{2}$, $\Delta y_{\gamma\gamma}$ being the difference between the two photon rapidities.
- 49 At lowest order, θ^* is the center-of-mass scattering angle of $q\bar{q} \rightarrow \gamma\gamma$ and $gg \rightarrow \gamma\gamma$
- 50 processes.

51 In addition, the integrated cross section is measured. The measurements refer to a kinematic
 52 acceptance requiring at least one isolated photon with $E_T > 23 \text{ GeV}$ and a second isolated
 53 photon with $E_T > 20 \text{ GeV}$, separated by $R > 0.45$. They are performed in two pseudorapidity
 54 regions, one with $|\eta| < 1.44$, and the other with $|\eta| < 2.5$ but excluding the transition region
 55 between the barrel and endcap calorimeters, $1.44 < |\eta| < 1.57$. For convenience the latter will
 56 be referred to as $|\eta| < 2.5$ throughout the paper.

57 Asymmetric thresholds were applied on the photon transverse momenta to avoid the infrared
 58 sensitivity affecting the fixed-order calculation [10, 11] and ease the comparison of the mea-
 59 surement with the theoretical prediction.

60 All simulations results are based on the PYTHIA 6.4.22 [12] event generator, Z2 tune [13],
 61 CTEQ6L PDF [14], and a GEANT 4 modelling of the detector. In simulation a prompt photon
 62 is considered as signal if the sum of the transverse momenta of the particles within a cone
 63 $R < 0.4$ around the photon direction is less than 5 GeV.

64 Event selection and background discrimination are presented in Sections 2 and 3. The deter-
 65 mination of the signal yield and the measurement of the cross-section will be explained in the
 66 Sections 4 and 5. Results are discussed in the Section 8 and compared with the theoretical
 67 predictions introduced in Section 7.

68 2 Event Selection

69 Photon candidates in CMS are reconstructed by clustering the energy deposited in the ECAL
 70 crystals [15, 16]. CMS is equipped with a versatile trigger to adapt to the LHC luminosity
 71 ramp-up. In this measurement three trigger settings were used for three successive data tak-
 72 ing periods. They require two photon candidates, with a threshold of either 15 GeV or 17 GeV
 73 on the transverse momentum of both candidates. For the last period, with the highest in-
 74 stantaneous luminosity, a weak isolation requirement was applied on one of the two photon
 75 candidates. For the three periods, the trigger efficiency for events passing the analysis selec-
 76 tions described in the following paragraphs is estimated from simulated events to be greater
 77 than 99.9%. The offline event selection requires one photon candidate with $E_T > 23 \text{ GeV}$ and
 78 a second photon candidate with $E_T > 20 \text{ GeV}$, each within the ECAL fiducial region (detector
 79 region covering $|\eta| < 1.44$ and $|\eta| > 1.57$) and within the tracker acceptance (detector region
 80 covering $|\eta| < 2.5$). The candidates are required to be separated by $R > 0.45$ to avoid overlap
 81 between their isolation region.

82 Photon identification criteria requiring the deposits in the calorimeters to be compatible with
 83 an electromagnetic shower are applied on the two candidates. The criteria are based on the
 84 spread along η of the energy clustered in the ECAL, henceforth referred to as $\sigma_{i\eta i\eta}$, and on the
 85 ratio H/E of the energy measured in HCAL and ECAL (see *loose selections* in Ref. [16]).

86 The photon candidates are required to be isolated. The sum of the transverse momenta of
 87 charged particles measured by the tracker and the sum of the transverse energy deposits in

88 HCAL, both defined within a cone of radius $R = 0.4$ around the photon direction, must each
 89 be less than 2 GeV in the barrel and 4 GeV in the endcaps. HCAL deposits in a cone of radius
 90 $R = 0.15$ are excluded from the sum as well as tracks in a cone of radius $R = 0.04$ and within
 91 a strip of $\Delta\eta = 0.03$ along the φ direction, which can potentially contain tracks of an electron-
 92 positron pair from a conversion of the photon in the tracker material. The sum of the transverse
 93 energy deposited in ECAL in a cone of radius $R = 0.3$ is required to be less than 20% of the
 94 photon transverse energy, in order to be consistent with the trigger requirements applied on-
 95 line. Excluded from the sum is the energy deposited within a cone of a radius corresponding
 96 to 3.5 crystals along η and within a 5-crystal-wide strip along φ . In addition, it is required that
 97 no charged particle with the following properties impinges on ECAL within a cone of radius
 98 $R = 0.4$: $p_T > 3$ GeV, impact parameters with regard to the primary vertex in the transverse
 99 and longitudinal planes of less than 1 mm and 2 mm, respectively, and associated with a hit in
 100 the innermost layer of the pixel detector. Tracks corresponding to such particles are henceforth
 101 called *impinging tracks*. The electron contamination is further reduced by imposing an addi-
 102 tional veto on the presence of hits in the layers of the pixel detector along the direction of the
 103 photon candidate.

104 3 Signal and Background Discrimination

105 After selection, candidate photons are either signal photons, background photons coming from
 106 hadron decays, the larger component coming from neutral meson decaying into a pair of
 107 collinear photons which is misidentified as a single one, or misidentified electrons. The back-
 108 grounds to diphotons are photon-jet and multi-jet events, with respectively one and two back-
 109 ground photons from neutral hadron decays, and Drell-Yan events, with two misidentified
 110 electrons.

111 The remaining contamination from Drell-Yan events is estimated from simulation using the
 112 next-to-leading order (NLO) POWHEG generator [17–19], which reproduces well our own
 113 measurement [20]. The diphoton cross-section measurement is corrected for this contamina-
 114 tion, which amounts to about 12% in the mass range 80 – 100 GeV around the Z peak. This
 115 procedure has a negligible impact on the systematic uncertainties.

116 Background photons from photon-jet and multi-jet events leave a wider footprint in ECAL than
 117 signal photons and are produced in jets alongside other particles, which also deposit energy in
 118 ECAL. An isolation variable \mathcal{I} based on the energy in the electromagnetic calorimeter is used to
 119 statistically estimate the fraction of diphoton events among the selected candidates. This vari-
 120 able is constructed to minimise the dependence on the energy deposited by minimum-ionising
 121 particles (MIPs) such that its distribution for the background can be obtained from data, the
 122 impinging-track method described thereafter, and it differs from the loose ECAL isolation used
 123 in the selection (see Section 2). It is defined as the sum of the transverse energy of the ECAL
 124 deposits with $E_T > 300$ MeV (MIPs veto), within a hollow cone centred on the photon impact
 125 point, of inner radius of 3.5 crystal edges and outer radius of $R = 0.4$. Deposits assigned to the
 126 photon itself or falling within a 5-crystal-wide strip along φ are removed. Thus, deposits from
 127 photons converting into electron-positron pairs in the tracker material being spread along φ do
 128 not contribute to the value of the electromagnetic isolation.

129 Since the distribution of \mathcal{I} is different for signal photons and background photons, this variable
 130 can be used in a maximum likelihood fit to extract the number of signal events in the entire
 131 selected sample. Fig. 1 shows the probability density function of \mathcal{I} , which was extracted from
 132 data with the methods described in the following.

133 Contributions to the value of the ECAL isolation variable for signal photons come from pile-up
 134 and underlying event activity. These contributions being independent of φ , the ECAL isolation
 135 probability density function $f(\mathcal{I})$ is estimated from *random cones* using events with at least one
 136 isolated photon candidate. The isolation variable \mathcal{I} is calculated in a cone of $R = 0.4$ around
 137 an axis at the same η as the photon candidate and at a random φ in a $\pi/2$ window around the
 138 axis perpendicular to the photon direction. The cone is also required not to include photon and
 139 electron candidates or jets. The ECAL isolation probability density function for signal photons
 140 is cross-checked with two additional independent methods, both exploiting e^+ and e^- , from Z
 141 and W boson decays, that do not radiate significantly in the tracker material, selected with a
 142 constraint on the fraction of bremsstrahlung energy emitted from the interaction in the tracker
 143 material is imposed. Such electrons and positrons leave ECAL energy deposits compatible
 144 with those of photons, and have a similar probability density function for \mathcal{I} . The $Z \rightarrow e^+e^-$
 145 events are selected with stringent requirements on the identification criteria of the lepton pair
 146 and on its invariant mass and the $f(\mathcal{I})$ distribution is obtained directly from both leptons. In
 147 $W \rightarrow e\nu$ events, $f(\mathcal{I})$ is obtained by exploiting the *sPlot* technique [21]. The missing transverse
 148 energy projected along the lepton axis is used to estimate the probability of an event to be
 149 signal ($W \rightarrow e\nu$) or background ($Z \rightarrow e^+e^-$, $W \rightarrow \tau\nu$, $\gamma + \text{jet(s)}$, QCD multijet processes) and
 150 the value of \mathcal{I} of the selected candidates is weighted accordingly, to estimate the distribution
 151 of \mathcal{I} . The uncertainty on $f(\mathcal{I})$ is taken to be the maximum difference between the distributions
 152 extracted from random cones and from electrons in Z and W events. In simulated events, the
 153 difference between $f(\mathcal{I})$ for signal photons and for random cones is lower than the uncertainty
 154 determined from data.

155 For background photons, $f(\mathcal{I})$ is extracted from a background sample with less than 0.1% of
 156 signal photons contamination. The sample is obtained by selecting photon candidates with one
 157 and only one impinging track. A cone of $R = 0.05$ around the track is excluded from the isola-
 158 tion area to avoid counting the energy deposited by the charged particle. The isolation variable
 159 \mathcal{I} is then normalised to the nominal isolation area. To validate this method, a distribution of
 160 \mathcal{I} is also extracted from a sample of events with two impinging tracks, one of the two being
 161 excluded in the computation of \mathcal{I} . The latter distribution is compared to the one obtained on
 162 the one-impinging-track sample, using the normal definition of \mathcal{I} , i.e. including the energy

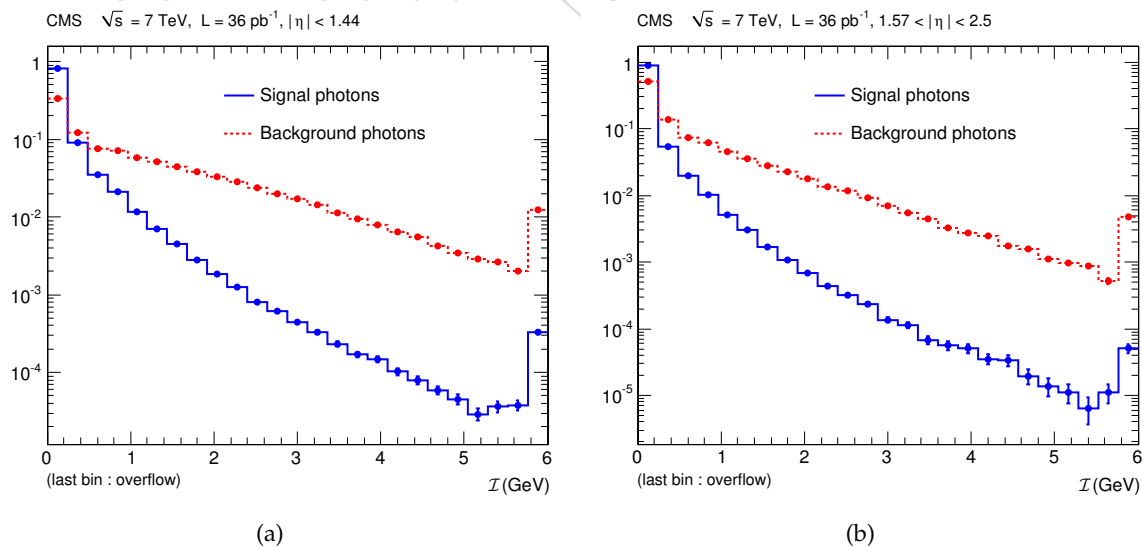


Figure 1: Probability density functions of \mathcal{I} for signal photons (solid blue) and background photons (dashed red) in the barrel (left) and in the endcap (right).

163 deposits in the vicinity of the track. The agreement is within one sigma in the entire range of
 164 the \mathcal{I} distribution and the difference is taken as a systematic uncertainty on the knowledge of
 165 $f(\mathcal{I})$ for background photons.

166 The distributions $f(\mathcal{I})$ show a moderate dependence on η and on the pile-up conditions, quan-
 167 tified by the number n_{vtx} of primary vertices in the events (2.4 on average). The background
 168 distribution $f(\mathcal{I})$ depends also on the transverse energy E_T of the candidate. Therefore, events
 169 in the sample used for the extraction of $f(\mathcal{I})$ are weighted to reproduce the distributions of η ,
 170 n_{vtx} , and E_T of the diphoton sample. The approximation made by using the diphoton sample
 171 in place of the signal and background distributions is taken into account in the systematic un-
 172 certainties. The distributions $f(\mathcal{I})$ for signal and background photons used in the maximum
 173 likelihood fit are shown in Fig. 1.

174 4 Signal Yield Determination

175 The number of diphoton events is obtained from a maximum-likelihood fit to the distributions
 176 of the ECAL isolation variables of the two photons, \mathcal{I}_1 and \mathcal{I}_2 , where numbers 1 and 2 are
 177 assigned randomly. Events are separated into three types: signal events ($\gamma\gamma$) if both photons
 178 are signal photons, background events with a signal photon and a background photon, and
 179 background events with two background photons.

180 The likelihood function \mathcal{L} maximised in the fit is

$$\mathcal{L} = \frac{e^{-N^{\text{tot}}}}{N!} \prod_{i=1}^N \sum_{t \in \mathcal{T}} N_t f_t(\mathcal{I}_1^i, \mathcal{I}_2^i), \quad (1)$$

181 where \mathcal{T} indicates the three event types, N is the event sample size, N_t are the numbers of
 182 events estimated in the fit for each type t , N^{tot} is their sum over the three event types, and
 183 $f_t(\mathcal{I}_1, \mathcal{I}_2)$ is the probability for the ECAL isolation variables of the two photons to have values
 184 \mathcal{I}_1 and \mathcal{I}_2 for the given event type t .

185 The probability density functions for the three event types are obtained by multiplying the
 186 probability density functions $f(\mathcal{I})$ for single photon candidates assuming the two statistical
 187 variables \mathcal{I}_1 and \mathcal{I}_2 to be independent. Correlations between these two variables have been
 188 checked with simulation and are small enough to be neglected.

189 The requirements described in Section 2 select 5977 events. These events are divided into three
 190 subsamples depending on whether both photons are in the barrel (2191 events), one is in the
 191 barrel and the other in the endcaps (2527 events), or both are in the endcaps (1259 events). The
 192 fit is performed separately for each of the three subsamples in each bin of each observable. An
 193 example of the fit for one bin of $m_{\gamma\gamma}$ spectrum is shown in Fig. 2 for events with both photons
 194 in the barrel ($|\eta| < 1.44$).

195 The maximum likelihood method is known to be biased for samples with small numbers of
 196 events. This bias is estimated with Monte-Carlo pseudo-experiments and the result of the fit
 197 corrected for it. It is less than 10% of the statistical error in 80% of the bins and never exceeds
 198 half the statistical error.

199 5 Cross-Section Measurement

200 The differential cross-section measurements $d\sigma/dX$, for the variable X in the interval X_i reads

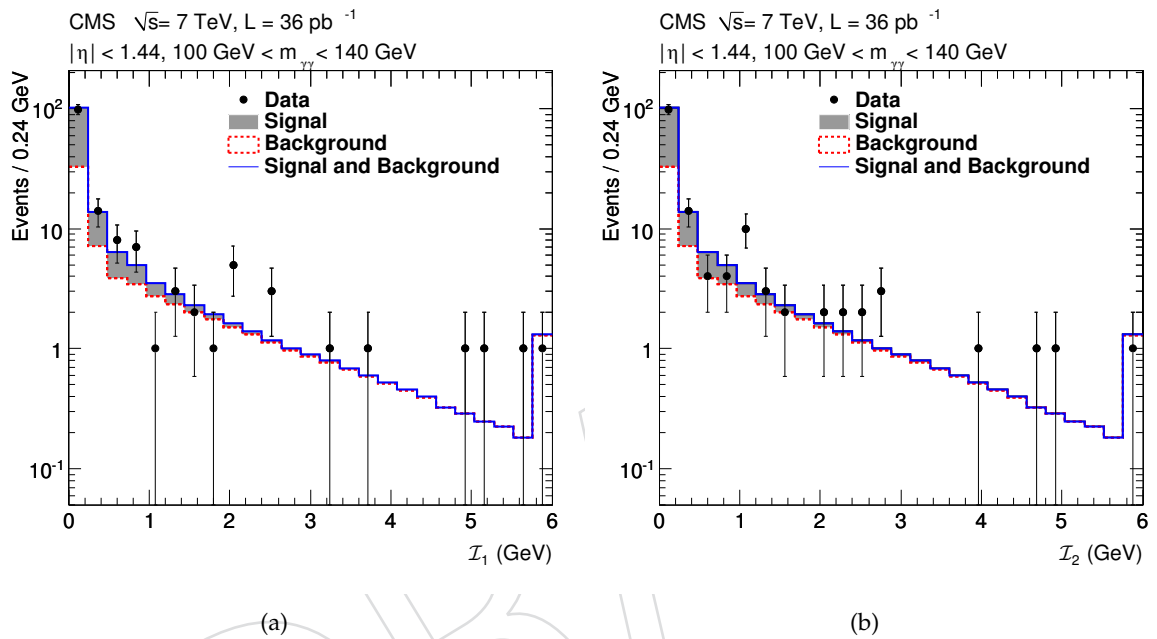


Figure 2: Fit of the photon ECAL isolation ($\mathcal{I}_1, \mathcal{I}_2$) in the bin $100 \text{ GeV} < m_{\gamma\gamma} < 140 \text{ GeV}$ for photons with $|\eta| < 1.44$. The distribution of the isolation variable \mathcal{I}_1 of one photon candidate, arbitrarily chosen as “first photon” and denoted with subscript ‘1’, is represented on the left figure together with the fit result, integrated over \mathcal{I}_2 : the dashed line represents the background contribution while the solid line the sum of the signal and background contributions. The same distributions for the second photon candidate is represented on the right figure. In this mass bin, with 161 selected candidates, the number of signal events is 72 ± 14 .

$$\frac{d\sigma}{dX}(X_i) = \frac{N_{\gamma\gamma}^U(X_i)}{\mathcal{L}\Delta X_i\mathcal{C}(X_i)}, \quad (2)$$

201 where $N_{\gamma\gamma}^U$ is the number of signal events unfolded for the detector resolution and corrected
 202 for the Drell-Yan contamination, \mathcal{L} the total integrated luminosity, ΔX_i the interval width, and
 203 \mathcal{C} a correction factor for the effects of the finite detector resolution on the acceptance and on the
 204 efficiencies of photon reconstruction and identification.

205 The number of signal events is unfolded for the detector resolution by inverting the response
 206 matrix T obtained from simulated events passing the selection requirements for $m_{\gamma\gamma}$, $p_{T,\gamma\gamma}$,
 207 $\Delta\phi_{\gamma\gamma}$, and $|\cos\theta^*|$. The matrix elements T^{ik} are the probabilities of a selected event with the
 208 generated value of X in bin X_k to be reconstructed with a value of X in bin X_i . For a given
 209 interval X_i , the number of events after unfolding is related to the observed numbers of events
 210 in the different intervals X_k by: $N_{\gamma\gamma}^U(X_i) = (T^{ik})^{-1}N_{\gamma\gamma}(X_k)$. Here, $N_{\gamma\gamma}(X_k)$ is the signal yield
 211 corrected for the Drell-Yan contamination as described in Sec. 3. Given the excellent perfor-
 212 mance of ECAL, the matrix is nearly diagonal and no regularisation is applied in the unfolding
 213 procedure.

The correction factor $\mathcal{C}(X_i)$ is defined as

$$\mathcal{C}(X_i) = \frac{N_{\text{reco}}^{\text{sim}}(X_i) \epsilon^{\text{data}}}{N_{\text{gen}}^{\text{sim}}(X_i) \epsilon^{\text{sim}}} \quad (3)$$

214 where

215 $N_{\text{reco}}^{\text{sim}}(X_i)$ is the number of simulated events passing all the selection criteria, with generated
 216 value of X within the interval X_i ;

217 $N_{\text{gen}}^{\text{sim}}(X_i)$ is the number of simulated events within the acceptance defined at generator level
 218 (Section 1), with generated values of X within the interval X_i ;

219 ϵ^{data} is the efficiency of the photon identification criteria measured from data;

220 ϵ^{sim} is the efficiency of the photon identification criteria obtained on simulated events using
 221 the same technique as for ϵ^{data} .

222 The efficiencies ϵ^{data} and ϵ^{sim} to observe a diphoton candidate are taken as the square of the
 223 efficiencies to observe a single photon.

224 The efficiency for the requirements on isolation, $\sigma_{i\eta i\eta}$, and H/E is estimated with a tag-and-
 225 probe method [22] applied to a $Z \rightarrow e^+e^-$ sample selected from the full CMS dataset collected
 226 in 2010. One lepton, the tag, is selected with tight reconstruction and identification criteria [23],
 227 while the other, the probe, is selected by requiring a constraint on the invariant mass of the
 228 lepton pair. The probes constitute a sample of unbiased electrons and positrons. The same
 229 constraint as the one discussed in Section 3 is applied on the fraction of bremsstrahlung energy
 230 emitted by the e^+ and e^- from the interaction in the tracker material. This ensures that the
 231 electromagnetic deposits of these “low-radiating” electrons and positrons are compatible with
 232 those of a photon shower. The efficiency is computed by applying the requirements on isola-
 233 tion, $\sigma_{i\eta i\eta}$, and H/E to this sample and is given by the fraction of probes passing the selection.

234 The efficiency for the requirement to have no impinging tracks within the isolation cone is es-
 235 timated from data, using a control sample built using a *random-cone* technique on events with
 236 a single photon selected according to the identification criteria described above. The random
 237 cone definition is the one introduced as in Section 3 for the extraction of $f(\mathcal{I})$. Particles within
 238 the random cone hence come mainly from pile-up and the underlying event. Therefore, quanti-
 239 ties such as the number of impinging tracks or energy deposits in the isolation area are assumed
 240 to be the same as for isolated photons. The efficiency of the requirement to have no imping-
 241 ing track within the isolation cone is given by the ratio of random cones passing this criteria
 242 to the total number of random cones. The efficiency of the veto on pixel hits is obtained from
 243 simulation. It is included in the $N_{\text{reco}}^{\text{sim}}/N_{\text{gen}}^{\text{sim}}$ term of expression (3).

244 The correction factor \mathcal{C} is $80.8 \pm 1.9\%$ for the integrated cross section in the region $|\eta| < 1.44$,
 245 and $76.2 \pm 3.3\%$ in the region $|\eta| < 1.44$ or $1.57 < |\eta| < 2.5$.

246 6 Systematic Uncertainties

247 The uncertainties on the reconstruction of the photon four-momentum are dominated by the
 248 ECAL energy scale, known at the level of 0.6% in the barrel and of 1.5% in the endcaps [24].
 249 This affects the definition of the acceptance and induces bin-to-bin migrations in the differential
 250 cross sections. The former impacts only kinematics regions near the photon p_T thresholds and
 251 results in an uncertainty of 40% in the most affected region, the lowest masses of $d\sigma/dm_{\gamma\gamma}$. The
 252 uncertainty from the bin-to-bin migration is about 1%.

253 The uncertainties associated with the photon identification efficiency include the statistical and
 254 systematic uncertainties added in quadrature. For the tag-and-probe and random-cone meth-
 255 ods, the systematic uncertainty is estimated by applying the respective methods on simulated
 256 data: the difference between the value obtained with the method and the value given by the
 257 fraction of simulated events passing the identification criterion is taken as systematic uncer-
 258 tainty. This estimate is conservative, considering that the efficiency calculation includes already
 259 a correction for this difference. The total uncertainties are 1.9% for diphotons in the barrel and
 3.3% for all diphotons.

Table 1: Different contributions to the systematic uncertainties on the measured differential cross sections. The systematic uncertainties are computed for each bin of Figures 3 to 10. In this table is listed the approximate value over the different bins.

Uncertainty source	$ \eta < 1.44$	$ \eta < 1.44$ or $1.57 < \eta < 2.5$
Energy scale on acceptance	1.5%	2%
Energy scale on bin-to-bin migration	1%	1.5%
Signal and background distribution, $f(\mathcal{I})$	7%	9%
Acceptance and efficiency correction factor, \mathcal{C}	2%	3%
Luminosity	4.0%	4.0%
Total	8%	11%

260

261 The impact of imperfect knowledge of the signal and background distributions $f(\mathcal{I})$ is esti-

262 mated with Monte Carlo pseudo-experiments where $f(\mathcal{I})$ are varied. The extent of the varia-
 263 tions corresponds to the discrepancies between the shapes of the principal and cross-check dis-
 264 tributions observed in the validation of the random-cone and impinging-track methods (Sec-
 265 tion 3). In the first bin of the probability density functions, they are of the order of ± 0.01 for
 266 the signal and range from ± 0.03 to ± 0.05 for the background. The uncertainty on the $f(\mathcal{I})$
 267 estimation from its dependence on the distribution of photon transverse momentum p_T , pho-
 268 ton pseudorapidity η , and number of vertices n_{vtx} is estimated by considering the change on
 269 $f(\mathcal{I})$ observed when using the p_T , η , and n_{vtx} distributions obtained from the diphoton sim-
 270 ulation instead of the ones from the diphoton event candidates. The effect of the latter on the
 271 measurement is negligible. The overall impact of the knowledge of the signal and background
 272 distributions on the integrated cross section is $\sim 8\%$, and varies from 4 to 27% on differential
 273 cross sections, depending on the bin and the subsample.

274 A 4% uncertainty is assigned to the integrated luminosity corresponding to the dataset [25].
 275 The various contributions to the systematic uncertainties are summarised in Table 1.

276 7 Theoretical Predictions

277 This Section introduces the theoretical calculations which are compared against the experimen-
 278 tal data in Section 8. The leading contributions to the production of pairs of prompt photons
 279 in pp collisions are the quark-antiquark annihilation ($q\bar{q} \rightarrow \gamma\gamma$), gluon fusion ($gg \rightarrow \gamma\gamma$), and
 280 gluon-(anti)quark scattering ($gq \rightarrow \gamma\gamma q$) processes. One or both photons come either directly
 281 from the hard process or from a parton fragmentation, a cascade of successive collinear split-
 282 tings ending up with a radiated photon. Contributions from the quark annihilation process
 283 and the single and double fragmentation processes are calculated up to order $\alpha_s\alpha^2$ with the
 284 DIPHOX 1.3.2 program [1]. The contributions from the gluon-fusion process $gg \rightarrow \gamma\gamma$, in-
 285 cluding the one-loop box of order $\alpha_s^2\alpha^2$, the interference between the one- and two-loop boxes,
 286 and the real emission one-loop ‘‘pentagon’’ $gg \rightarrow \gamma\gamma g$, both of order $\alpha_s^3\alpha^2$, are calculated with
 287 the GAMMA2MC 1.1.1 program [2]. The fragmentation function BFG set II [26] has been used
 288 in the calculation. Although being higher-order processes, the gluon-fusion contributions are
 289 quantitatively comparable to those from quark-antiquark annihilation in the mass range of in-
 290 terest (including the region pertinent to the $H \rightarrow \gamma\gamma$ search), due to the significant gluon lumi-
 291 nosity in this range at the LHC. The three theoretical scales, normalisation, initial factorisation,
 292 and fragmentation, are set to the diphoton mass value.

293 The photons are required to be within the kinematic acceptance defined in Section 1. An ad-
 294 ditional isolation requirement at the parton level is imposed by requiring the total hadronic
 295 transverse energy deposited in a cone of radius 0.4 centred on the photon to be less than
 296 5 GeV. Particles resulting from underlying event activity and hadronisation are not included
 297 in partonic event generators such as DIPHOX and GAMMA2MC. The fraction of diphotons
 298 not selected due to underlying hadronic activity falling inside the isolation cone is estimated
 299 using the PYTHIA 6.4.22 [12] event generator with the tunes D6T [27], Z2 [13], P0 [28], and
 300 DWT [27]. The parton-level cross section is corrected by a factor 0.95 ± 0.04 .

301 The uncertainties associated with the limited knowledge of the parton distribution functions
 302 (PDFs) and the strong coupling constant α_s are determined according to the PDF4LHC rec-
 303 ommendations [29]. The cross section is computed with three different PDF sets (CT10 [30],
 304 MSTW08 [31], and NNPDF21 [32]) taking into account their associated uncertainties and the
 305 uncertainties on α_s . The respective preferred α_s central value of the PDF sets is used and α_s
 306 is varied within ± 0.012 . The value for the cross section is taken as the mid-point of the enve-
 307 lope of the three results, including the errors. The error on the cross section is taken to be the

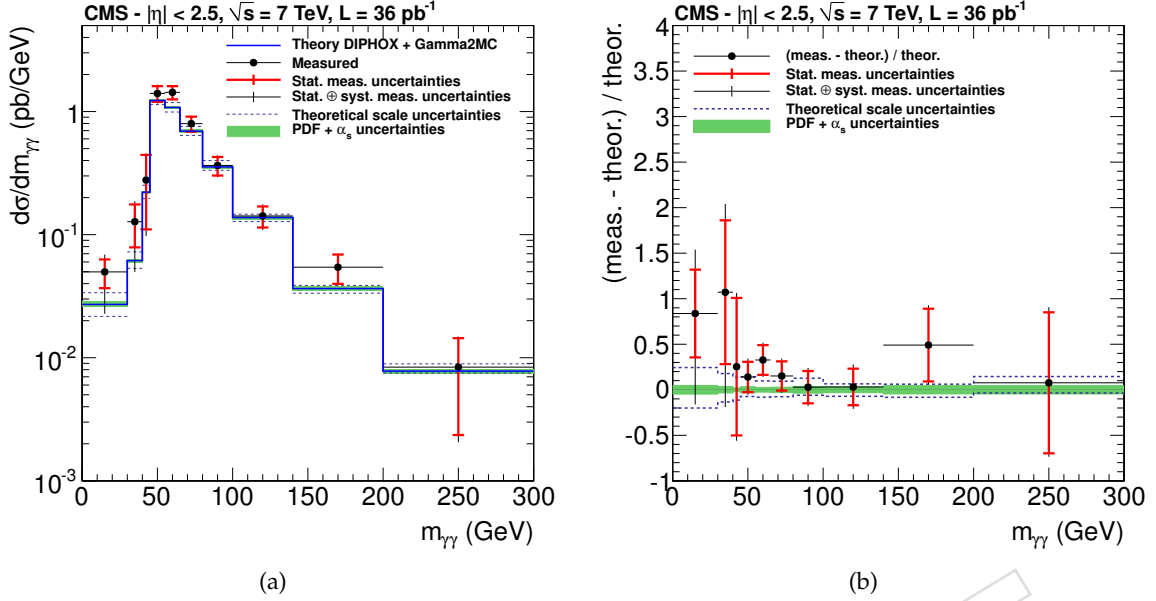


Figure 3: Measured cross section of diphoton production as (a) a function of the invariant mass of the photon pair and (b) bin-by-bin comparison with the theory for photons within the pseudorapidity region $|\eta| < 1.44$ or $1.57 < |\eta| < 2.5$. The uncertainty from the luminosity measurement, not included in the error bars, is 4%.

308 envelope.

309 The theoretical scale uncertainties are estimated by varying the normalisation, initial factorisation, and fragmentation scales by factors of 1/2 and 2, keeping the ratio between two scales less
 310 than 2 (for instance the combination $0.5 m_{\gamma\gamma}, 2 m_{\gamma\gamma}, m_{\gamma\gamma}$ is not considered). The uncertainty is
 311 taken to be the maximum difference in the obtained cross sections.
 312

313 8 Results

The integrated cross sections obtained for the acceptance defined in Section 2 are:

$$\begin{aligned}\sigma(pp \rightarrow \gamma\gamma)|_{|\eta| < 1.44} &= 31.0 \pm 1.8 \text{ (stat)} \begin{matrix} +2.0 \\ -2.1 \end{matrix} \text{ (syst)} \pm 1.2 \text{ (lumi)} \text{ pb}, \\ \sigma(pp \rightarrow \gamma\gamma)|_{|\eta| < 2.50} &= 62.4 \pm 3.6 \text{ (stat)} \begin{matrix} +5.3 \\ -5.8 \end{matrix} \text{ (syst)} \pm 2.5 \text{ (lumi)} \text{ pb}.\end{aligned}$$

The calculation performed as described in previous section predicts,

$$\begin{aligned}\sigma(pp \rightarrow \gamma\gamma)|_{|\eta| < 1.44} &= 27.3 \begin{matrix} +3.0 \\ -2.2 \end{matrix} \text{ (scales)} \pm 1.1 \text{ (PDF)} \text{ pb}, \\ \sigma(pp \rightarrow \gamma\gamma)|_{|\eta| < 2.50} &= 52.7 \begin{matrix} +5.8 \\ -4.2 \end{matrix} \text{ (scales)} \pm 2.0 \text{ (PDF)} \text{ pb}.\end{aligned}$$

314 The integrated cross-sections obtained from the calculation are compatible with the measure-
 315 ments within the experimental and theoretical uncertainties.

316 The differential cross-section measurements for the two considered pseudorapidity ranges are
 317 shown along with the theoretical predictions in Figures 3 through 10. The uncertainty from
 318 the luminosity, not included in the error bars, is 4%. The values of the cross sections for each
 319 bin are provided in Tables 2 to 5. As can be seen in Fig. 7 and Fig. 8, the prediction underes-
 320 timates the measured cross section for $\Delta\phi_{\gamma\gamma} < 2.8$. In the leading-order (LO) term of gluon
 321 fusion and quark annihilation $2 \rightarrow 2$ processes, the two photons are back-to-back because of

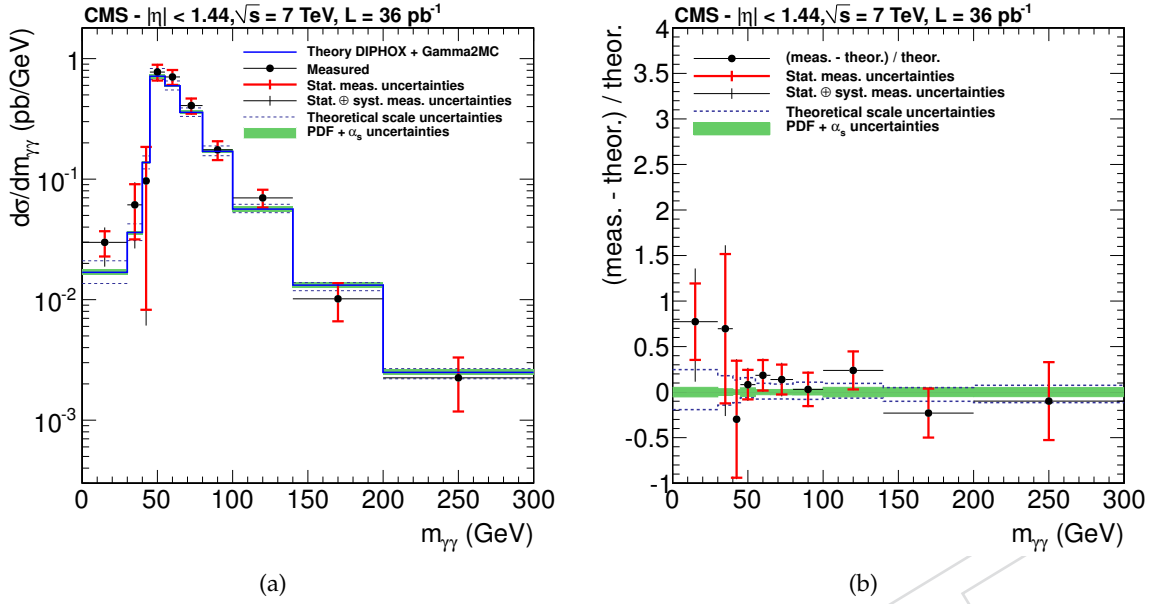


Figure 4: Measured cross section of diphoton production (a) as a function of the invariant mass of the photon pair and (b) bin-by-bin comparison with the theory for photons within the pseudorapidity region $|\eta| < 1.44$. The total systematic uncertainties are represented by the shaded area, the different contributions are added in quadrature sequentially. The uncertainty from the luminosity measurement, not included in the error bars, is 4%.

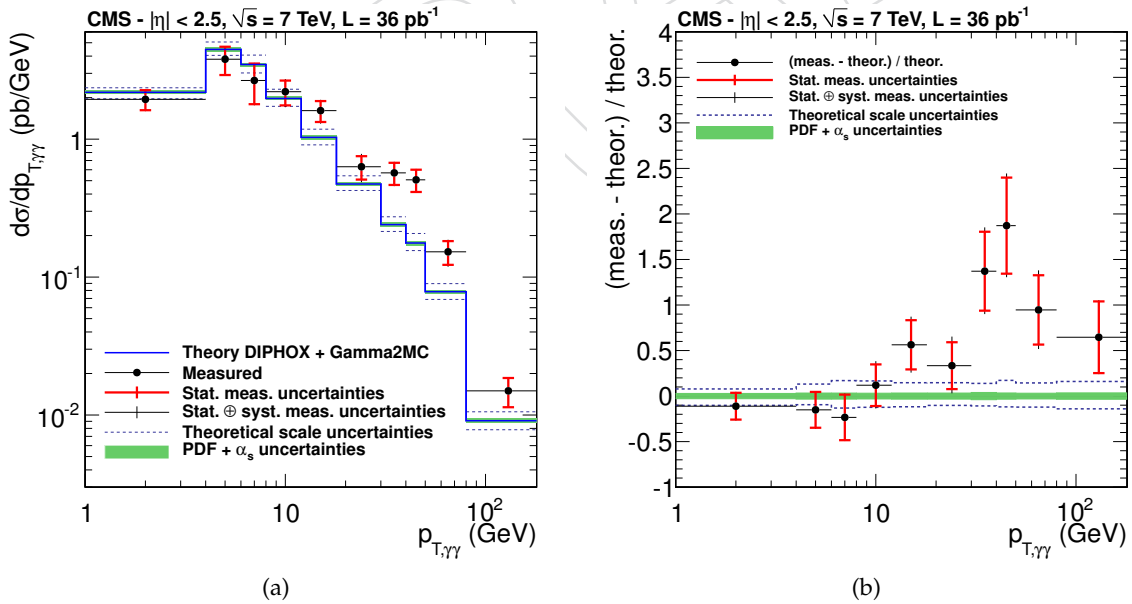


Figure 5: Measured cross section of diphoton production (a) as a function of the transverse momentum of the photon pair and (b) bin-by-bin comparison with the theory for photons within the pseudorapidity region $|\eta| < 1.44$ or $1.57 < |\eta| < 2.5$. The uncertainty from the luminosity measurement, not included in the error bars, is 4%.

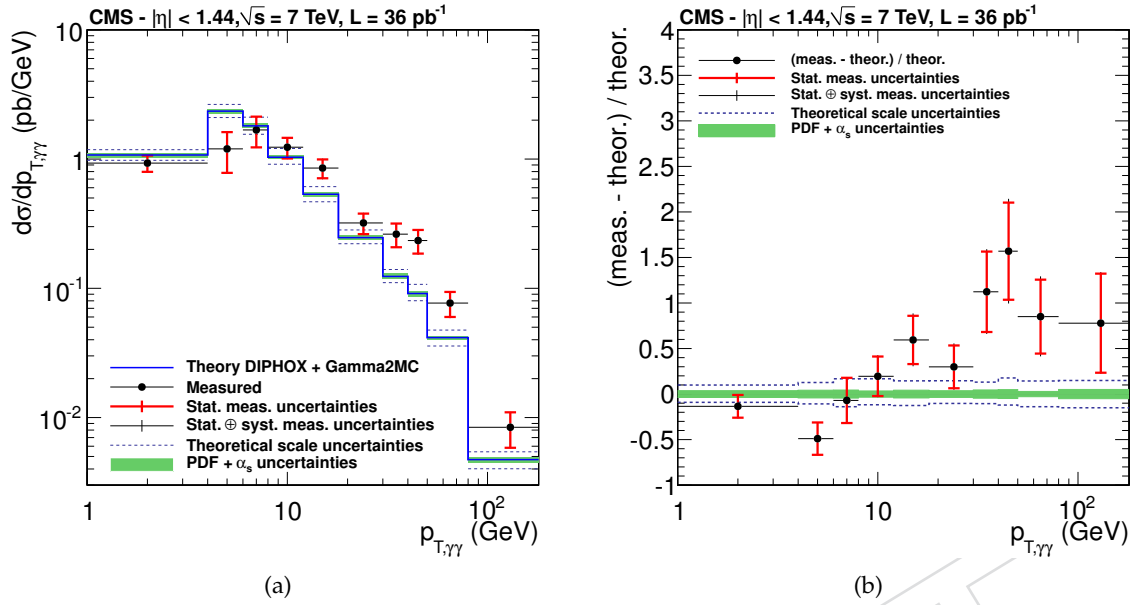


Figure 6: Measured cross section of diphoton production (a) as a function of the transverse momentum of the photon pair and (b) bin-by-bin comparison with the theory for photons within the pseudorapidity region $|\eta| < 1.44$. The uncertainty from the luminosity measurement, not included in the error bars, is 4%.

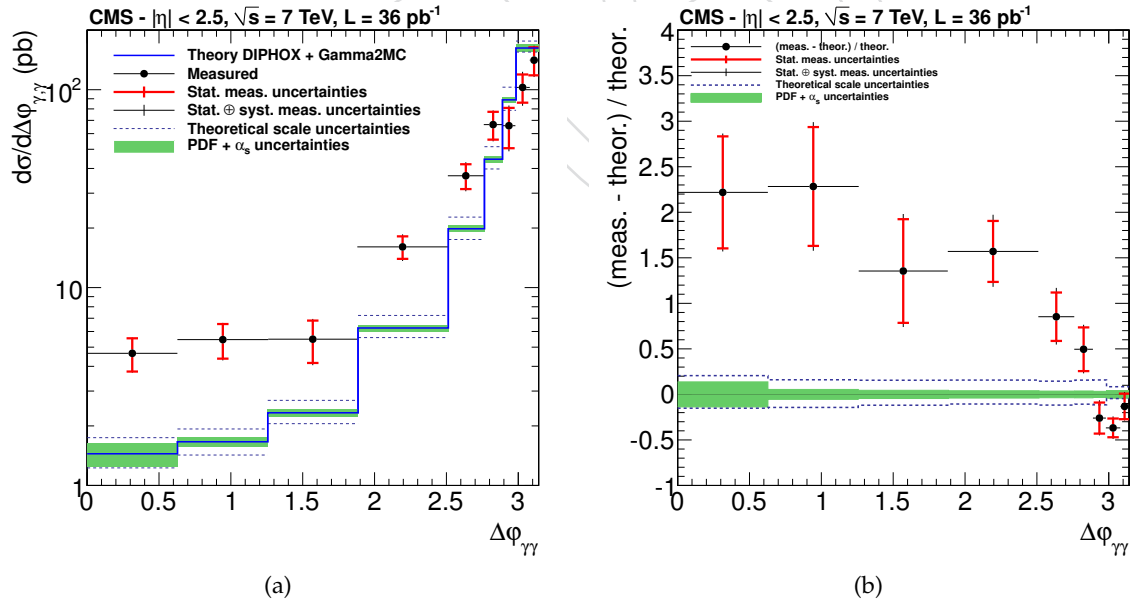


Figure 7: Measured cross section of diphoton production (a) as a function of the azimuthal angle between the two photons and (b) bin-by-bin comparison with the theory (b) for photons within the pseudorapidity region $|\eta| < 1.44$ or $1.57 < |\eta| < 2.5$. The uncertainty from the luminosity measurement, not included in the error bars, is 4%.

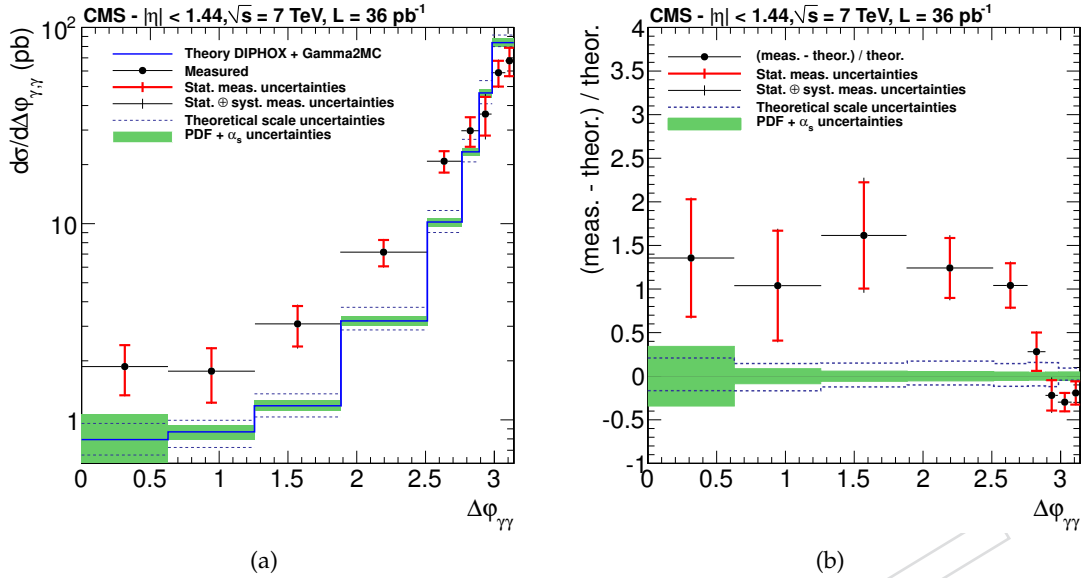


Figure 8: Measured cross section of diphoton production (a) as a function of the azimuthal angle between the two photons and (b) bin-by-bin comparison with the theory for photons within the pseudorapidity region $|\eta| < 1.44$. The uncertainty from the luminosity measurement, not included in the error bars, is 4%.

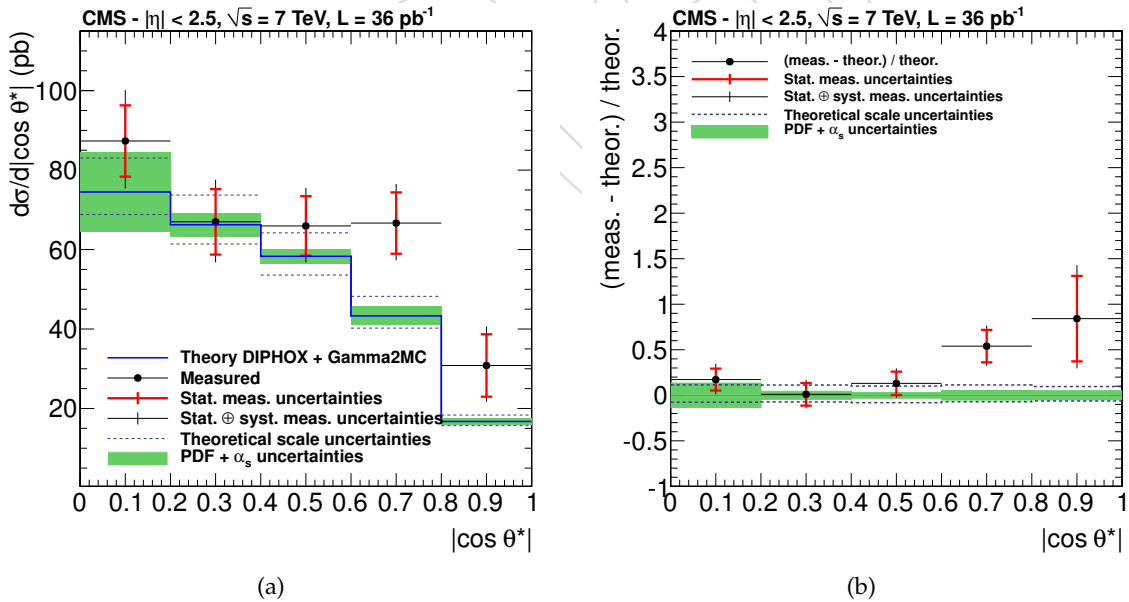


Figure 9: Measured cross section of diphoton production (a) as a function of $\cos\theta^* = \tanh\frac{\eta}{2}$ and (b) bin-by-bin comparison with the theory for photons within the pseudorapidity region $|\eta| < 1.44$ or $1.57 < |\eta| < 2.5$. The uncertainty from the luminosity measurement, not included in the error bars, is 4%.

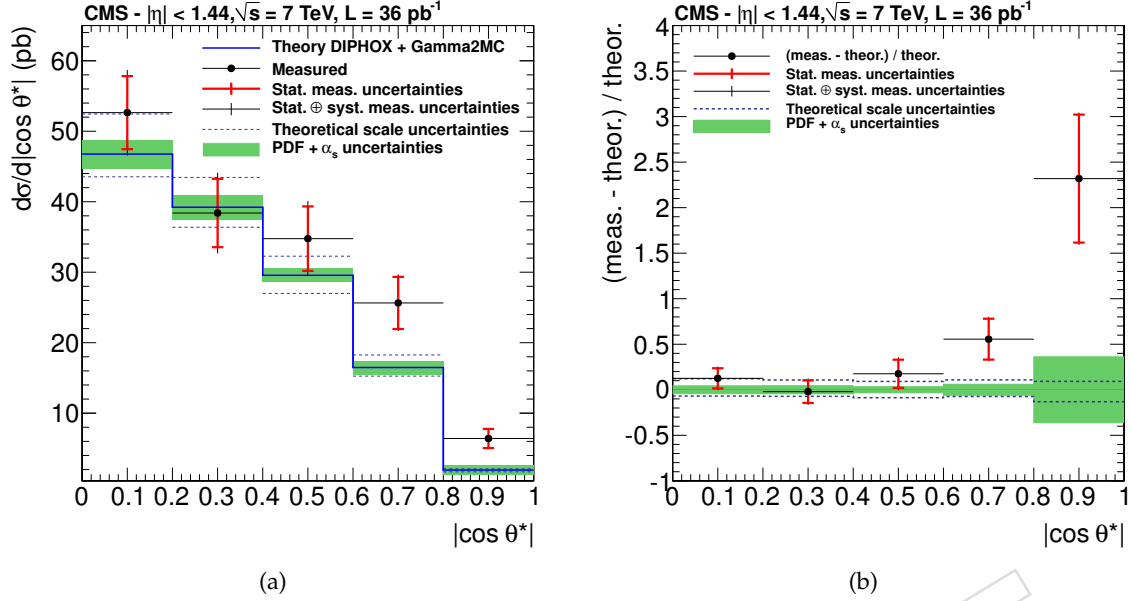


Figure 10: Measured cross section of diphoton production as (a) a function of $\cos\theta^* = \tanh\frac{\eta}{2}$ and (b) bin-by-bin comparison with the theory for photons within the pseudorapidity region $|\eta| < 1.44$. The last bin of the histogram, $0.8 < |\cos\theta^*| < 1$, is only populated up to $|\cos\theta^*| < 0.95$, limit resulting from the $|\eta|$ boundary. The uncertainty from the luminosity measurement, not included in the error bars, is 4%.

322 momentum conservation. Therefore the LO term does not contribute to this phase space re-
 323 gion, which is effectively covered in the NLO calculation by only one order for both direct and
 324 fragmentation production. The contribution for $\Delta\varphi_{\gamma\gamma} \lesssim \pi$, combined with the requirements of
 325 $E_T > 20, 23$ GeV on the two photons, is responsible for the shoulder in the vicinity of 40 GeV
 326 observed in the diphoton E_T distribution of Fig. 5 and Fig. 6. This contribution also populates
 327 the region below 30 GeV in the diphoton mass distribution shown in Fig. 3 and Fig. 4. In these
 328 two regions of the $p_{T,\gamma\gamma}$ and $m_{\gamma\gamma}$ spectra, the calculated cross section is lower than the mea-
 329 surement, consistently with the deficit for $\Delta\varphi_{\gamma\gamma} < 2.8$. This disagreement provides valuable
 330 input for the calculation of processes not covered by current theoretical predictions.

331 Comparison of the measurements of the $\cos\theta^* = \tanh\frac{\eta}{2}$ spectrum shown Fig. 9 and Fig. 10
 332 shows an underestimation from the theory of the large $\cos\theta^*$ value, especially significant for
 333 the central part ($\eta < 1.44$).

334 Similar discrepancies have already been observed in the diphoton production at hadron collid-
 335 ers [5, 8, 33] and discussed in Ref. [34].

Table 2: Measured cross section of diphoton production as a function of the variable $m_{\gamma\gamma}$ with statistical (stat.) and systematic uncertainties (sys.).

$d\sigma/dm_{\gamma\gamma}$ [pb/ GeV]								
$m_{\gamma\gamma}$ [GeV]	$ \eta < 1.44$				$ \eta < 1.44$ or $1.57 < \eta < 2.5$			
	stat.	sys.	stat.	sys.	stat.	sys.	stat.	sys.
0–30	0.0299	± 0.0071	+0.0069	–0.0086	0.050	± 0.013	+0.014	–0.024
30–40	0.061	± 0.030	+0.015	–0.018	0.127	± 0.049	+0.035	–0.061
40–45	0.097	± 0.088	+0.020	–0.020	0.28	± 0.17	+0.065	–0.067
45–55	0.77	± 0.12	+0.062	–0.054	1.40	± 0.20	+0.14	–0.12
55–65	0.705	± 0.10	+0.046	–0.039	1.43	± 0.18	+0.10	–0.093
65–80	0.408	± 0.059	+0.030	–0.031	0.80	± 0.11	+0.070	–0.065
80–100	0.175	± 0.031	+0.013	–0.012	0.365	± 0.063	+0.041	–0.037
100–140	0.070	± 0.012	+0.0035	–0.0034	0.142	± 0.028	+0.020	–0.018
140–200	0.0102	± 0.0035	+6.9E-4	–6.4E-4	0.054	± 0.015	+0.0065	–0.0059
200–300	0.0022	± 0.0011	+9.8E-5	–8.7E-5	0.0084	± 0.0060	+0.0023	–0.0019

Table 3: Measured cross section of diphoton production as a function of the variable $p_{T,\gamma\gamma}$ with statistical (stat.) and systematic uncertainties (sys.).

$d\sigma/dp_{T,\gamma\gamma}$ [pb/ GeV]								
$p_{T,\gamma\gamma}$ [GeV]	$ \eta < 1.44$				$ \eta < 1.44$ or $1.57 < \eta < 2.5$			
	stat.	sys.	stat.	sys.	stat.	sys.	stat.	sys.
0–4	0.93	± 0.13	+0.044	–0.047	1.94	± 0.32	+0.12	–0.13
4–6	1.20	± 0.42	+0.097	–0.085	3.80	± 0.88	+0.27	–0.29
6–8	1.68	± 0.45	+0.12	–0.12	2.66	± 0.87	+0.27	–0.24
8–12	1.24	± 0.22	+0.083	–0.076	2.21	± 0.45	+0.26	–0.22
12–18	0.85	± 0.14	+0.065	–0.062	1.61	± 0.28	+0.15	–0.15
18–30	0.320	± 0.058	+0.026	–0.022	0.63	± 0.12	+0.089	–0.076
30–40	0.262	± 0.055	+0.019	–0.017	0.57	± 0.10	+0.050	–0.044
40–50	0.234	± 0.049	+0.02	–0.019	0.507	± 0.093	+0.040	–0.036
50–80	0.077	± 0.017	+0.0073	–0.0067	0.153	± 0.030	+0.016	–0.016
80–180	0.0084	± 0.0026	+6.0E-4	–5.2E-4	0.0150	± 0.0036	+0.0010	–8.6E-4

Table 4: Measured cross section of diphoton production as a function of the variable $\Delta\phi_{\gamma\gamma}$ with statistical (stat.) and systematic uncertainties (sys.).

$d\sigma/d\Delta\phi_{\gamma\gamma}$ [pb]								
$\Delta\phi_{\gamma\gamma}$	$ \eta < 1.44$				$ \eta < 1.44$ or $1.57 < \eta < 2.5$			
		stat.	sys.		stat.	sys.		
$0-\pi/5$	1.87	± 0.53	+0.13	-0.13	4.65	± 0.89	+0.29	-0.30
$\pi/5-2\pi/5$	1.77	± 0.55	+0.15	-0.14	5.5	± 1.1	+0.45	-0.45
$2\pi/5-3\pi/5$	3.09	± 0.72	+0.31	-0.29	5.5	± 1.3	+0.61	-0.54
$3\pi/5-4\pi/5$	7.2	± 1.1	+0.49	-0.44	16.1	± 2.1	+1.4	-1.2
$4\pi/5-0.88\pi$	20.8	± 2.6	+1.0	-0.96	36.7	± 5.3	+3.4	-3.0
$0.88\pi-0.92\pi$	29.8	± 5.1	+1.7	-1.5	67	± 11	+5.4	-5.0
$0.92\pi-0.95\pi$	36.2	± 8.1	+5.1	-4.7	66	± 15	+8.6	-7.6
$0.95\pi-0.98\pi$	58.8	± 8.8	+4.2	-3.8	103	± 17	+12	-11
$0.98\pi-\pi$	68	± 11	+3.9	-3.8	141	± 23	+12	-11

Table 5: Measured cross section of diphoton production as a function of the variable $\cos\theta^*$ with statistical (stat.) and systematic uncertainties (sys.).

$d\sigma/d\cos\theta^*$ [pb]								
$\cos\theta^*$	$ \eta < 1.44$				$ \eta < 1.44$ or $1.57 < \eta < 2.5$			
		stat.	sys.		stat.	sys.		
$0-0.2$	52.6	± 5.2	+3.1	-3.2	87.3	± 9.0	+9.1	-7.9
$0.2-0.4$	38.4	± 4.9	+3.0	-3.0	67.0	± 8.2	+6.6	-6.0
$0.4-0.6$	34.8	± 4.6	+2.7	-2.5	66.0	± 7.5	+5.9	-5.3
$0.6-0.8$	25.6	± 3.7	+1.6	-1.5	66.7	± 7.7	+6.1	-5.3
$0.8-1$	6.4	± 1.4	+0.34	-0.36	30.8	± 7.9	+5.9	-4.7

9 Conclusions

The integrated and differential production cross sections of isolated photon pairs have been measured in proton-proton collisions at a centre-of-mass energy of 7 TeV, using data collected by the CMS detector in 2010, corresponding to an integrated luminosity of 36 pb^{-1} . The differential cross sections have been measured as functions of the diphoton invariant mass, the diphoton transverse momentum, the difference of the two photon azimuthal angles, and the $\cos \theta^* = \tanh \frac{y}{2}$ observable. The background contamination from hadron decay products is estimated with a statistical method based on an electromagnetic energy isolation variable \mathcal{I} . The signal and background distributions for \mathcal{I} have been entirely extracted from data resulting in systematic uncertainties of approximately 10% on the measured diphoton yield.

The measurements have been compared to a theoretical prediction performed at next-to-leading-order accuracy using the state-of-the-art fixed order computations [1, 2]. Whereas there is an overall agreement between data and theory for the mass spectrum, the theoretical cross section appears underestimated for regions of the phase space where the two photons are not collinear.

Acknowledgements

We wish to express our gratitude to J-Ph. Guillet, E. Pilon, Z. Bern, L. Dixon, and C. Schmidt for the fruitful discussions on the theoretical aspects concerning the measurement.

We wish to congratulate our colleagues in the CERN accelerator departments for the excellent performance of the LHC machine. We thank the technical and administrative staff at CERN and other CMS institutes, and acknowledge support from: FMSR (Austria); FNRS and FWO (Belgium); CNPq, CAPES, FAPERJ, and FAPESP (Brazil); MES (Bulgaria); CERN; CAS, MoST, and NSFC (China); COLCIENCIAS (Colombia); MSES (Croatia); RPF (Cyprus); Academy of Sciences and NICPB (Estonia); Academy of Finland, MEC, and HIP (Finland); CEA and CNRS/IN2P3 (France); BMBF, DFG, and HGF (Germany); GSRT (Greece); OTKA and NKTH (Hungary); DAE and DST (India); IPM (Iran); SFI (Ireland); INFN (Italy); NRF and WCU (Korea); LAS (Lithuania); CINVESTAV, CONACYT, SEP, and UASLP-FAI (Mexico); MSI (New Zealand); PAEC (Pakistan); SCSR (Poland); FCT (Portugal); JINR (Armenia, Belarus, Georgia, Ukraine, Uzbekistan); MST and MAE (Russia); MSTD (Serbia); MICINN and CPAN (Spain); Swiss Funding Agencies (Switzerland); NSC (Taipei); TUBITAK and TAEK (Turkey); STFC (United Kingdom); DOE and NSF (USA). Individuals have received support from the Marie-Curie programme and the European Research Council (European Union); the Leventis Foundation; the A. P. Sloan Foundation; the Alexander von Humboldt Foundation; the Associazione per lo Sviluppo Scientifico e Tecnologico del Piemonte (Italy); the Belgian Federal Science Policy Office; the Fonds pour la Formation à la Recherche dans l'Industrie et dans l'Agriculture (FRIA-Belgium); the Agentschap voor Innovatie door Wetenschap en Technologie (IWT-Belgium); and the Council of Science and Industrial Research, India.

References

- 372 [1] T. Binoth et al., "A full next-to-leading order study of direct photon pair production in
373 hadronic collisions", *Eur. Phys. J.* **C16** (2000) 311, arXiv:hep-ph/9911340.
374 doi:10.1007/s100520050024.
375
- 376 [2] Z. Bern, L. J. Dixon, and C. Schmidt, "Isolating a light Higgs boson from the di-photon
377 background at the LHC", *Phys. Rev.* **D66** (2002) 074018, arXiv:hep-ph/0206194.
378 doi:10.1103/PhysRevD.66.074018.
- 379 [3] V. Saleev, "Diphoton production at Tevatron in the quasi-multi-Regge-kinematics
380 approach", *Phys. Rev.* **D80** (2009) 114016, arXiv:0911.5517.
381 doi:10.1103/PhysRevD.80.114016.
- 382 [4] C. Balazs et al., "Calculation of prompt diphoton production cross sections at Tevatron
383 and LHC energies", *Phys. Rev.* **D76** (2007) 013009, arXiv:0704.0001.
384 doi:10.1103/PhysRevD.76.013009.
- 385 [5] D0 Collaboration, "Measurement of direct photon pair production cross sections in $p\bar{p}$
386 collisions at $\sqrt{s} = 1.96$ TeV", *Phys. Lett.* **B690** (2010) 108, arXiv:1002.4917.
387 doi:10.1016/j.physletb.2010.05.017.
- 388 [6] CDF Collaboration, "Measurement of the Cross Section for Prompt Isolated Diphoton
389 Production in $p\bar{p}$ Collisions at $\sqrt{s} = 1.96$ TeV", *Phys. Rev. Lett.* **107** (2011) 102003.
390 doi:10.1103/PhysRevLett.107.102003.
- 391 [7] CDF Collaboration, "Measurement of the cross section for prompt isolated diphoton
392 production in $p\bar{p}$ collisions at $\sqrt{s} = 1.96$ TeV", *Phys. Rev.* **D84** (2011) 052006.
393 doi:10.1103/PhysRevD.84.052006.
- 394 [8] ATLAS Collaboration, "Measurement of the isolated di-photon cross-section in pp
395 collisions at $\sqrt{s} = 7$ TeV with the ATLAS detector", arXiv:1107.0581.
- 396 [9] CMS Collaboration, "The CMS experiment at the CERN LHC", *JINST* **03** (2008) S08004.
397 doi:10.1088/1748-0221/3/08/S08004.
- 398 [10] S. Frixione and G. Ridolfi, "Jet photoproduction at HERA", *Nucl. Phys.* **B507** (1997) 315,
399 arXiv:hep-ph/9707345. doi:10.1016/S0550-3213(97)00575-0.
- 400 [11] M. Fontannaz, J. Guillet, and G. Heinrich, "Is a large intrinsic $k(T)$ needed to describe
401 photon + jet photoproduction at HERA?", *Eur. Phys. J.* **C22** (2001) 303,
402 arXiv:hep-ph/0107262. doi:10.1007/s100520100797.
- 403 [12] T. Sjöstrand, S. Mrenna, and P. Skands, "PYTHIA 6.4 Physics and Manual", *JHEP* **05**
404 (2006) 026, arXiv:hep-ph/0603175. doi:10.1088/1126-6708/2006/05/026.
- 405 [13] R. Field, "Early LHC Underlying Event Data - Findings and Surprises", *The PYTHIA6*
406 *Z2 tune is identical to the Z1 tune described in this reference, except that Z2 uses the CTEQ6L*
407 *PDF while Z1 uses CTEQ5L* arXiv:1010.3558.
- 408 [14] J. Pumplin, D. Stump, J. Huston et al., "New generation of parton distributions with
409 uncertainties from global QCD analysis", *JHEP* **07** (2002) 012,
410 arXiv:hep-ph/0201195.

-
- 411 [15] CMS Collaboration, "Photon Reconstruction and Identification at $\sqrt{s} = 7$ TeV",
412 *CMS-PAS-EGM-10-005* (2010).
- 413 [16] CMS Collaboration, "Isolated Photon Reconstruction and Identification at $\sqrt{s} = 7$ TeV",
414 *CMS-PAS-EGM-10-006* (2010).
- 415 [17] S. Alioli et al., "A general framework for implementing NLO calculations in shower
416 Monte Carlo programs: the POWHEG BOX", *JHEP* **06** (2010) 043,
417 arXiv:1002.2581. doi:10.1007/JHEP06(2010)043.
- 418 [18] S. Frixione, P. Nason, and C. Oleari, "Matching NLO QCD computations with Parton
419 Shower simulations: the POWHEG method", *JHEP* **11** (2007) 070,
420 arXiv:0709.2092. doi:10.1088/1126-6708/2007/11/070.
- 421 [19] P. Nason, "A new method for combining NLO QCD with shower Monte Carlo
422 algorithms", *JHEP* **11** (2004) 040, arXiv:hep-ph/0409146.
423 doi:10.1088/1126-6708/2004/11/040.
- 424 [20] CMS Collaboration, "Measurement of the Drell-Yan Cross Section in pp Collisions at
425 $\sqrt{s} = 7$ TeV", arXiv:1108.0566. * Temporary entry *.
- 426 [21] M. Pivk and F. R. Le Diberder, "sPlot: a statistical tool to unfold data distributions",
427 *Nucl. Instrum. Meth.* **A555** (2005) 356, arXiv:physics/0402083.
428 doi:10.1016/j.nima.2005.08.106.
- 429 [22] CMS Collaboration, "Measurements of Inclusive W and Z Cross Sections in pp Collisions
430 at $\sqrt{s} = 7$ TeV", *JHEP* **1101** (2011) 080, arXiv:1012.2466. * Temporary entry *.
431 doi:10.1007/JHEP01(2011)080.
- 432 [23] CMS Collaboration, "Electron Reconstruction and Identification at $\sqrt{s} = 7$ TeV",
433 *CMS-PAS-EGM-10-004* (2010).
- 434 [24] CMS Collaboration, "ECAL 2010 performance results", *CMS Detector Performance*
435 *Summary CMS-DPS-2011-008* (2011).
- 436 [25] CMS Collaboration, "Measurement of CMS Luminosity", *CMS-DP-2011-002. Document*
437 *in preparation* (2011).
- 438 [26] L. Bourhis, M. Fontannaz, J. Guillet et al., "Next-to-leading order determination of
439 fragmentation functions", *Eur. Phys. J.* **C19** (2001) 89, arXiv:hep-ph/0009101.
440 doi:10.1007/s100520100579.
- 441 [27] CDF Collaboration, "Studying the 'underlying event' at CDF and the LHC", in
442 *Proceedings of the First International Workshop on Multiple Partonic Interactions at the LHC*
443 *MPI08* (2009) 12.
- 444 [28] P. Z. Skands, "Tuning Monte Carlo Generators: The Perugia Tunes", *Phys. Rev.* **D82**
445 (2010) 074018, arXiv:1005.3457. doi:10.1103/PhysRevD.82.074018.
- 446 [29] M. Botje et al., "The PDF4LHC Working Group Interim Recommendations",
447 arXiv:1101.0538.
- 448 [30] H.-L. Lai et al., "New parton distributions for collider physics", *Phys. Rev.* **D82** (2010)
449 074024, arXiv:1007.2241. doi:10.1103/PhysRevD.82.074024.

- 450 [31] A. D. Martin et al., “Parton distributions for the LHC”, *Eur. Phys. J.* **C63** (2009) 189,
451 arXiv:0901.0002. doi:10.1140/epjc/s10052-009-1072-5.
- 452 [32] R. D. Ball et al., “Impact of Heavy Quark Masses on Parton Distributions and LHC
453 Phenomenology”, arXiv:1101.1300.
- 454 [33] CDF Collaboration, “Measurement of the Cross Section for Prompt Isolated Diphoton
455 Production in $p\bar{p}$ Collisions at $\sqrt{s} = 1.96\text{TeV}$ ”, arXiv:1106.5123.
- 456 [34] T. Binoth et al., “Beyond leading order effects in photon pair production at the Tevatron”,
457 *Phys. Rev.* **D63** (2001) 114016, arXiv:hep-ph/0012191.
458 doi:10.1103/PhysRevD.63.114016.

DRAFT